

See discussions, stats, and author profiles for this publication at: <https://www.researchgate.net/publication/221773589>

# Role of Defects in the Phase Transition of VO<sub>2</sub> Nanoparticles Probed by Plasmon Resonance Spectroscopy

ARTICLE *in* NANO LETTERS · FEBRUARY 2012

Impact Factor: 13.59 · DOI: 10.1021/nl203782y · Source: PubMed

CITATIONS

57

READS

116

7 AUTHORS, INCLUDING:



**Kannatassen Appavoo**

Brookhaven National Laboratory

35 PUBLICATIONS 320 CITATIONS

SEE PROFILE



**Dangyuan Lei**

The Hong Kong Polytechnic University

78 PUBLICATIONS 1,182 CITATIONS

SEE PROFILE



**Stefan Maier**

Imperial College London

310 PUBLICATIONS 12,945 CITATIONS

SEE PROFILE



**Richard F Haglund**

Vanderbilt University

378 PUBLICATIONS 5,917 CITATIONS

SEE PROFILE

# Role of defects in the phase transition of VO<sub>2</sub> nanoparticles probed by plasmon resonance spectroscopy

Kannatassen Appavoo,<sup>\*,†,‡,⊥</sup> Dang Yuan Lei,<sup>⊥</sup> Yannick Sonnefraud,<sup>§</sup> Bin Wang,<sup>||</sup> Sokrates T. Pantelides,<sup>||,#</sup> Stefan A. Maier,<sup>§</sup> and Richard F. Haglund, Jr.<sup>†,‡,||</sup>

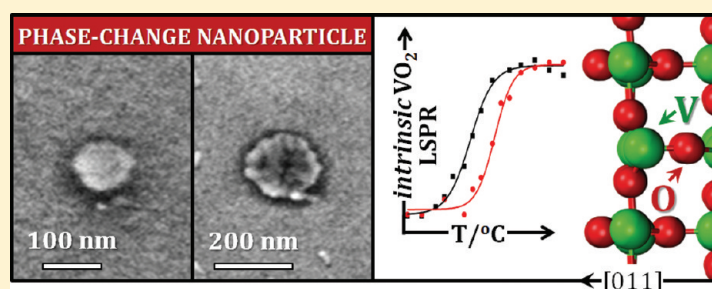
<sup>†</sup>Interdisciplinary Program in Materials Science and <sup>‡</sup>Institute for Nanoscale Science and Engineering, Vanderbilt University, Nashville, Tennessee 37235-0106, United States

<sup>§</sup>Department of Physics, Imperial College London, London SW7 2AZ, United Kingdom

<sup>||</sup>Department of Physics and Astronomy, Vanderbilt University, Nashville, Tennessee 37235-1807, United States

<sup>#</sup>Materials Science and Technology Division, Oak Ridge National Laboratory, Oak Ridge, Tennessee 37831, United States

## S Supporting Information



**ABSTRACT:** Defects are known to affect nanoscale phase transitions, but their specific role in the metal-to-insulator transition in VO<sub>2</sub> has remained elusive. By combining plasmon resonance nanospectroscopy with density functional calculations, we correlate decreased phase-transition energy with oxygen vacancies created by strain at grain boundaries. By measuring the degree of metallization in the lithographically defined VO<sub>2</sub> nanoparticles, we find that hysteresis width narrows with increasing size, thus illustrating the potential for domain boundary engineering in phase-changing nanostructures.

**KEYWORDS:** Vanadium dioxide, VO<sub>2</sub>, phase transition, interface, defect, size effect, localized surface plasmon resonance, density functional theory, domain boundary engineering

Atomic and electronic reconstructions in phase-changing materials (PCMs) are increasingly considered for nanoscale data storage, switching, and photonics technologies. Such device technologies rely on switchable modification of the electrical and optical properties of PCMs when heat, laser pulses, or electrical fields are applied to overcome the energy barrier to the phase transformation.<sup>1</sup> As these devices are scaled down, a deeper understanding of entangled structural and electronic effects is essential to tailoring the functionality of PCM devices. Of particular interest are surfaces, grain boundaries, and interfaces of PCM nanostructures owing to their pronounced contribution at the nanoscale. Recent examples are conduction at an insulator surface,<sup>2</sup> superconductivity at oxide interfaces,<sup>3</sup> and reduced switching energies in interfacial PCMs.<sup>4</sup>

One of the most widely studied, indeed canonical, PCMs is vanadium dioxide (VO<sub>2</sub>), which in thin-film form is being considered for applications in ultrafast switches,<sup>5</sup> modulating barriers in multilayered spin switches,<sup>6</sup> Mott field-effect transistors,<sup>7</sup> and novel solid-state memory devices.<sup>8</sup> VO<sub>2</sub> undergoes a first-order phase transformation near room temperature. At the critical temperature ( $T_c$ ) of 68 °C,

insulating monoclinic (M1; space group  $P2_1/C$ ) VO<sub>2</sub> transforms to a metallic rutile (R; space group  $P4_2/mnm$ ) crystallographic configuration so that this structural phase transition is accompanied by an electronic phase transition.<sup>9,10</sup> Perhaps even more technologically relevant than this tunable near-room-temperature switching is the fact that the structural transformation in VO<sub>2</sub> can also occur in less than 100 fs when triggered by a laser pulse.<sup>11</sup> Despite the simple stoichiometry and structure of VO<sub>2</sub> however, there are many unresolved puzzles about its metal-to-insulator transition (MIT), such as, the mechanism of ultrafast switching,<sup>12</sup> the potential for stabilizing the intermediate M2 phase,<sup>13</sup> the origins of size-dependent switching in VO<sub>2</sub> nanoparticles (NPs),<sup>14,15</sup> and nanoscale electronic and structural phase coexistence in thermally modulated VO<sub>2</sub>.<sup>16</sup> Additionally, the specific origins of metallicity at grain boundaries have also emerged as a critical issue for PCM applications involving the transport and electrical properties of VO<sub>2</sub>.<sup>17–21</sup> Unfortunately, it is precisely

Received: October 26, 2011

Revised: January 10, 2012

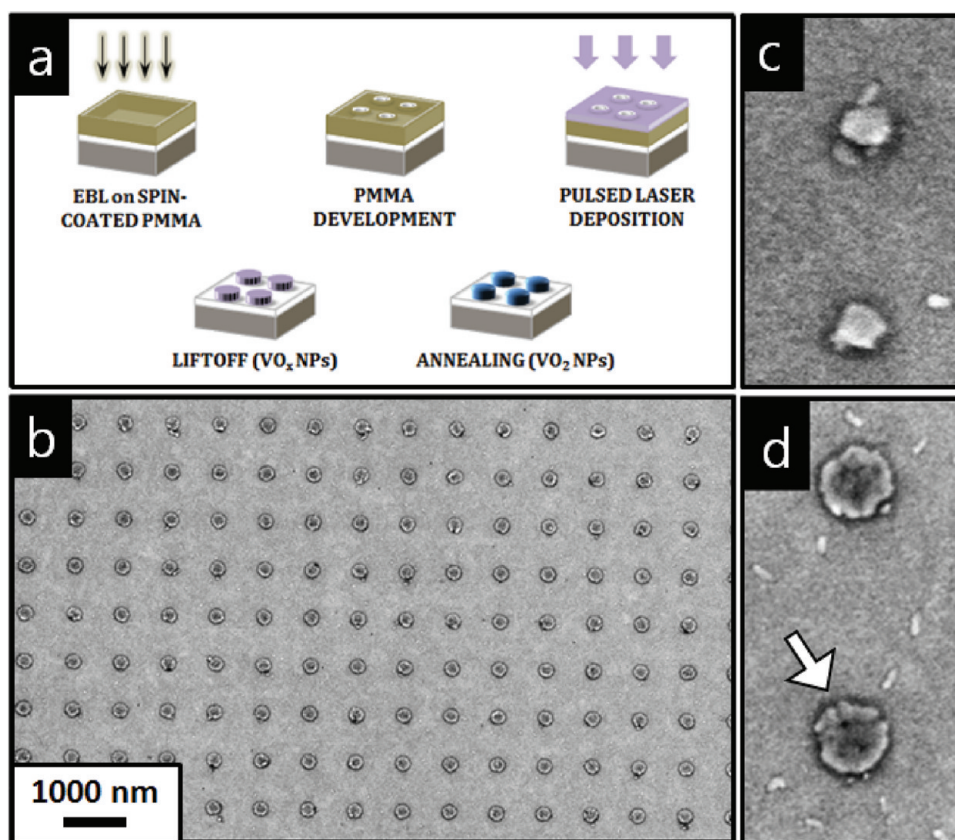


**Figure 1.** Fabrication and characterization of pristine  $\text{VO}_2$  nanostructures. (a) Schematic of the fabrication method. (b) SEMs of  $\text{VO}_2$  NPs depicting integrity of the arrays. Panels (c) and (d) show the smallest ( $r = 48$  nm) and largest ( $r = 105$  nm) nanostructures in this study, respectively. Note not only the individual NP characteristics arising in the annealing process but also the presence of multiple grains/boundaries (dark line) in (d) indicated by the arrow. All SEMs were acquired at an accelerating voltage of 3 kV and working distance of 7 mm for better resolution of surface morphology.

that knowledge of the specific point defects that nucleate this phase transition which is not available.

In this paper, we show that the most likely point defect nucleating the phase transition is an oxygen vacancy present at grain boundaries. By lithographically defining the size of the NPs, we constrain the number of grain boundaries in each NP from none to only a few, thus controlling the relative number of point defects that can be thermally activated in this heterogeneous nucleation process.<sup>22</sup> Here, in contrast to the recent work of Fan et al. showing the effect of mesoscopic twin boundaries on the MIT in strained  $\text{VO}_2$  microbeams, we focus on determining the nature of the initiating point defect by tracking the MIT in  $\text{VO}_2$  NPs that are few orders of magnitude smaller in volume than the microbeams.<sup>23</sup> Thus, interfacial effects within individual  $\text{VO}_2$  NPs – solely due to grain boundaries and facet mismatch – can be evaluated from the switching properties of  $\text{VO}_2$  PCM. By tracking the dipolar plasmonic response of the  $\text{VO}_2$  NPs as they metallize near  $T_c$ , we observe a systematic decrease in hysteresis width with increasing particle size and number of grain boundaries (see pairs of arrows in Figure 2b–d illustrating the definition of this width). This corresponds to a decreased energy barrier for the phase transition.

The dipolar character of this plasmon resonance is confirmed by using 3D full-wave finite-difference time-domain (FDTD) calculations. Density-functional calculations show that the strain associated with the larger NPs favors the formation of oxygen vacancies in grain boundaries as the defect responsible for heterogeneously nucleating the phase transformation.<sup>24</sup>

These results have significant implications for the understanding not only of PCM properties at nanometer length scales, but also of polycrystalline and epitaxial thin films, where interaction among the various crystallites can have a profound macroscopic effect on the character of the MIT.

**Experiments and Simulations.** We fabricated arrays of nanodisks with varying lateral dimensions on the same ITO-covered glass substrate by means of: (i) electron beam lithography (EBL: 10 kV accelerating voltage, 12.5 pA beam current, and  $95 \mu\text{C}/\text{cm}^2$  nominal dosage) in a spin-coated layer of poly(methyl-methacrylate) (PMMA: 200 nm thick); followed by (ii) chemical removal of the exposed regions; (iii) pulsed laser deposition (PLD:  $\lambda = 248$  nm, 25 ns pulse duration,  $3.84 \text{ J}/\text{cm}^2$  fluence, 10 Hz repetition rate, vanadium metal target, and 10 mTorr of  $\text{O}_2$  gas) of amorphous, substoichiometric  $\text{VO}_2$  (40 nm  $\text{VO}_{x=1.7}$  nominal thickness); and (iv) thermal anneal (450 °C,  $\text{O}_2$  gas at 250 mTorr for 20 min) to render the NPs crystalline and stoichiometric. As the  $\text{VO}_2$  NPs crystallized during the annealing process, they also acquired some individual variations in morphology<sup>25</sup> so as to contain a single domain or few grains, depending on the restriction imposed on their volume and shape by the lithographic process. Ordered arrays were used to enhance the signal-to-noise level while particle–particle interactions were minimized. This was achieved by keeping the grating period to ratio ( $L/r$ ) constant and more than a factor of 5 ( $L/r \sim 6.0$  here), which normalized the scattering cross-section per unit coverage area, proportional to  $(r/L)^2$ , and minimized near-field interactions, respectively.<sup>14,26,27</sup> As shown from the

scanning electron micrographs (SEMs) in Figure 1, the largest NPs ( $r = 105$  nm) exhibit multiple grain boundaries within individual NPs that contain point defects, dislocations, and other structural imperfections. For the array containing the smallest NPs ( $r = 48$  nm) however, the NPs appear to consist mostly of single grains.

The extinction spectrum of each array was acquired in an inverted optical microscope (Bruker Hyperion 2000) integrated with a Fourier-transform infrared spectrometer (Bruker Vertex 70) as follows: (i) the  $100 \times 100 \mu\text{m}^2$  array of interest was positioned under white-light uniform illumination from a tungsten lamp, focused by a reflective objective (36 $\times$  and NA 0.5) onto the substrate side of the sample; (ii) light transmitted through the array was selected by an aperture and collected by another reflective objective (36 $\times$  and NA 0.5) that was also used to adjust the focus on the sample surface and detected by an InGaAs photodiode; (iii) the transmission spectrum from an uncoated area close to the particle array was also collected for normalizing the array measurement; (iv) the sample was then heated using a Peltier cooler mounted on the stage or allowed to cool, and the measurement sequence was then repeated at the next temperature plateau where the focus was once again checked. Spectra were acquired at intervals of about 3  $^\circ\text{C}$ , yielding about 30 data points per cycle for each array. Figure 2

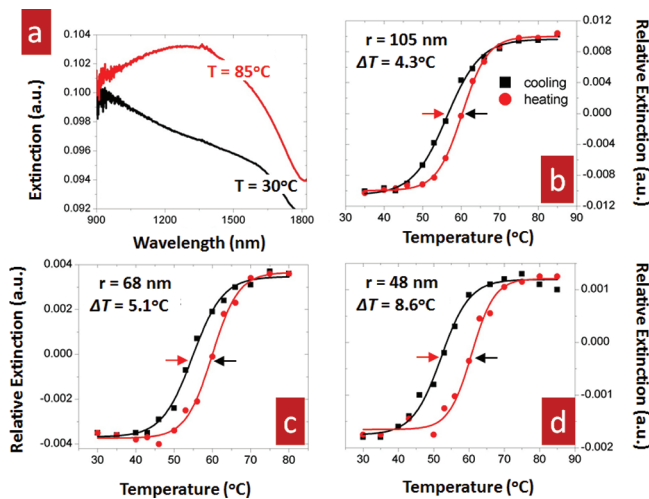


**Figure 2.** Localized surface plasmon resonance in  $\text{VO}_2$  nanostructures. (a) Typical plasmonic response of  $\text{VO}_2$  nanostructures as a function of wavelength in their metallic (red) and insulating (black) state for the  $r = 105$  nm nanoparticle case. For each set of spectra, plasmonic hysteresis curves of the relative extinction intensities were plotted for the different nanoparticle arrays with nominal lateral dimension of (b)  $r = 105$ , (c)  $r = 68$ , and (d)  $r = 48$  nm. The fits were obtained by using two sigmoidal functions, red for the heating sides and black for the cooling ones, while pairs of arrows in (b–d) depict hysteresis widths obtained.

depicts the resulting intrinsic plasmonic hystereses for the arrays.

In the metallic phase, the real part of the  $\text{VO}_2$  dielectric function becomes negative around  $1.1 \mu\text{m}$ .<sup>28</sup> According to the Fröhlich condition in first approximation,<sup>29</sup> the dipolar plasmon resonance of  $\text{VO}_2$  NPs occurs when  $\text{Re}\{\epsilon_{\text{VO}_2}\} = 2\epsilon_d$ , where  $\epsilon_d$  is the dielectric constant of the nanoparticle environment. Here the effective  $\epsilon_d$  lies between the dielectric constant of the substrate ( $\sim 2.25$ ) and air ( $\sim 1$ ), which leads to

an expected dipolar plasmon mode for the  $\text{VO}_2$  NPs between 1.3 and  $1.8 \mu\text{m}$ , consistent with the experimentally observed response of the NPs. Figure 2b–d presents hysteresis curves at the relative extinction intensity, defined as  $\sigma = \sigma_{\text{ext}}(\lambda = \text{resonance}) - \sigma_{\text{ext}}(\lambda = 1100 \text{ nm})$ , that is, the difference between the two extinction values at the on- and off-resonant wavelengths. It is seen from Figure 2b–d that the hysteresis width increases substantially as the nanoparticle radius decreases. This trend can be explained by the fact that defects and dislocations around the grain boundaries in bigger NPs act as nucleation sites for this heterogeneous phase transition, thus reducing the energy requirement as quantified by the width of the thermal hysteresis. In contrast to the work by Donev et al.,<sup>25</sup> highlighting the stochastic nature of the MIT in  $\text{VO}_2$  through the study of single NPs, this work aims at understanding the average effect of size and homointerfaces. The effect of grain orientation (with respect to the substrate) has also been suppressed due to the nonpreferential crystal growth orientation on glass substrate. In such an array configuration, the NPs domain alignment is randomized, that is, their domains do not all align in the same direction. Consequently, this minimizes any strain contribution from the substrate.

Moreover, the dipolar resonance substantially redshifts with the increase of particle radius as plotted in Figure 3c. Indeed, as the  $\text{VO}_2$  nanoparticles have transformed from their insulating to metallic states, they behave similarly to metal nanoparticles with a characteristic plasmon resonance, albeit a strongly damped resonance. Thus, as the nanoparticles become larger, the retardation effect on the exciting field increases over the volume of the nanoparticle, leading to a shift in the plasmon resonance. Intuitively, this can also be understood by realizing that since the distance between the charges at opposite interfaces of the particle increases with size, a smaller restoring force is required, which lowers the resonance frequency and hence accounts for the observed redshift.<sup>29</sup> In order to gain deeper understanding of the measured wavelength dependence of the dipolar plasmon resonance on the particle shape, FDTD simulations were carried out using Lumerical FDTD Solutions. The FDTD calculations simulated a single  $\text{VO}_2$  nanostructure ( $x, y, z = 0$  nm) of varying radial dimensions with periodic boundary conditions and a grid meshing size of 2 nm. While one monitor was placed above the nanostructure at  $z = 100$  nm to record transmission of the white-light pulse ( $x$  polarized), another monitor ( $z = 10$  nm) was used to record the spatial near-field enhancements. Since the three-dimensional morphology of the nanoparticle cannot be exactly determined, two independent sets of simulations were carried out to correlate the shape effect with the nanostructure plasmonic response. While the first set of simulations calculated the response of hemispherical nanoparticle, the second set simulated nanodisks. The thickness of both structures was set at 32 nm, the average value found by atomic force microscopy. The simulated spectra of Figure 3a clearly reproduce the heavily damped dipole response of metallic  $\text{VO}_2$  nanostructures (red curves) in the near IR region. As the nanoparticle size increases (from 96 to 210 nm in diameter), we observe the characteristic redshift with the increased size of the NPs. Moreover, the simulation matches well with experiments by Lopez et al. experiments,<sup>14</sup> with greater scattering amplitude in the visible for the nanoparticle in an insulating state (only shown here for the 96 nm insulating  $\text{VO}_2$  NP, blue curve). As their plasmonic dipolar resonances, confirmed by the field plots in Figure 3b,



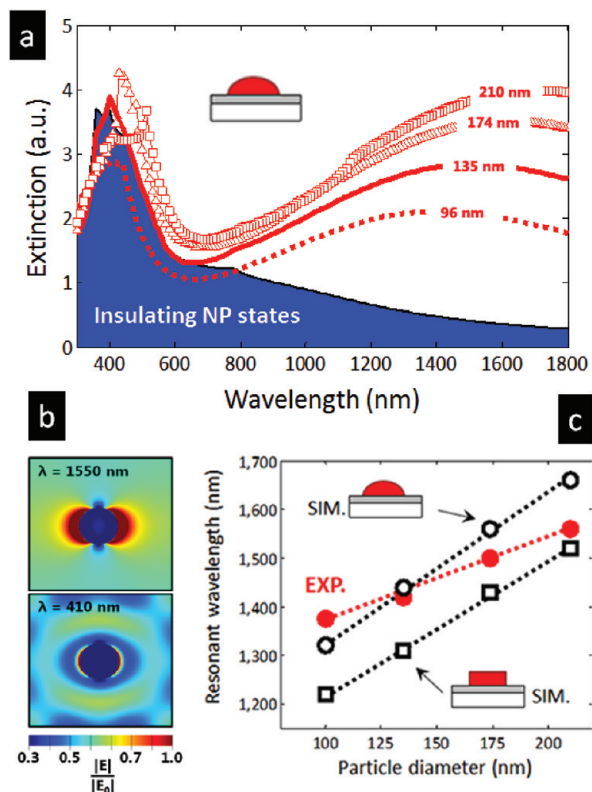


**Figure 3.** Electromagnetic response of  $\text{VO}_2$  nanostructures from FDTD simulations. (a) Extinction spectra of  $\text{VO}_2$  hemispheres in their metallic (red) and insulating (96 nm only shown, blue) states. (b) Nanoscale spatial distribution of electromagnetic fields at wavelengths of 410 and 1550 nm for the metallic  $\text{VO}_2$  NPs depicting the two resonance modes of the system. (c) Plasmon resonance wavelength as a function of particle diameter for the two sets of simulations (hemispherical and discoidal structures). Experimental measurements are superimposed in red. The  $\text{VO}_2$  dielectric constants were extracted from ref 10.

are plotted for the two sets of simulations in Figure 3c, we find that the simulated hemispherical NPs better fit the experimental results for smaller NPs. However, as NP size increases, the discoidal simulations agree better with experiments. This suggests that annealing tends to round off the smaller NPs but retains the original disk-like shape for bigger NPs, possibly due to the variation in wetting behavior for the larger-area nanodisks. Such morphological changes due to annealing are also visible in the high-resolution atomic force micrographs (see Supporting Information, Figure S1).

In order to gain insight about size and interface effects on switching, we plot in Figure 4 the hysteresis widths—corresponding to the energy requirement—of the electronic (circles) and structural (squares) phase transitions as a function of the  $\text{VO}_2$  volume for nanoparticles and thin-film samples grown using the same pulsed-laser deposition protocol.<sup>30</sup> First, one can clearly see that the structural signature always has a larger hysteresis width than its electronic counterpart, both in pristine (green, black, and red) and gold-interfaced (yellow)  $\text{VO}_2$  systems. Since the phenomenon occurs even at the single domain level, one might attribute this noncongruence to the intrinsic structure of the  $\text{VO}_2$  rather than to any dimensional effect. From a thermodynamic perspective, such a discrepancy also makes sense, because an atomic rearrangement should have a higher energy cost than a change in electronic structure. Moreover, since the mechanism represents a combination of the electronic correlation (Mott–Hubbard) together with a structural (Peierls) contribution, this difference in energy expenditure corresponds potentially to the two correlation lengths of the phase transformation.<sup>31</sup>

Furthermore, an interfacial effect is clearly apparent in Figure 4. In the single domain regime, for example, a gold heterointerface ( $\text{Au}/\text{VO}_2$ ) has the effect of reducing the hysteresis width by  $\sim 25$  and 18 K for the structural and electronic transitions, respectively. A similar interface effect is apparent in the multidomain regime as well, where the homointerface ( $\text{VO}_2$ – $\text{VO}_2$  grain boundary) narrows the hysteresis width by about 22 K. We can deduce therefore

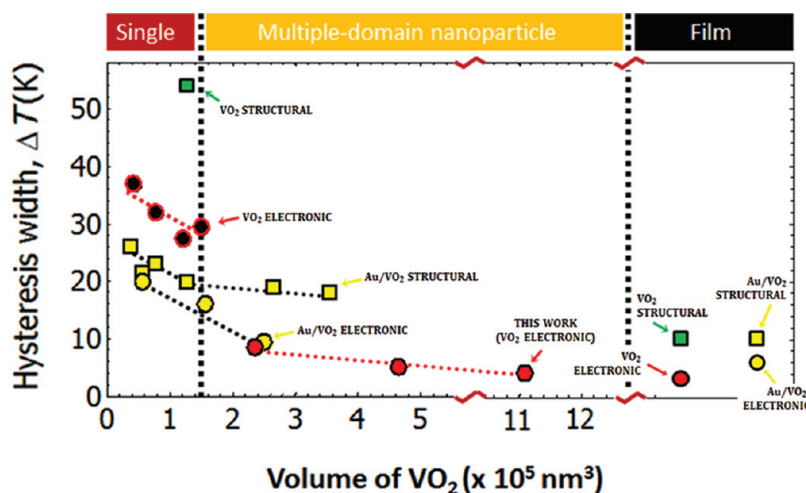


**Figure 4.** Hysteresis widths as a function of  $\text{VO}_2$  volume for three distinct regions: single domain, multidomain NPs, and film, separated by bold, vertical dotted lines. Circles represent data collected from measurements of the electronic transition (extinction or scattering), while square data were from measurements of the structural transition (Raman or XRD). In the single and multidomain nanoparticle regimes, data points were extracted from refs 14 (circles, red border, black fill), 25 (square, green fill, black border), 32 (squares, yellow fill, black border), and 15 (circles, yellow fill, black border). In the film region (green and red fill) data were extracted from ref 33, while the yellow-filled square and circle were obtained from refs 32 and 34, respectively. The lines serve as guides to the eyes.

that the formation of a single grain boundary is sufficient to lower the energy required to effect the transition due to an increase of point defects that can act as nucleation sites. The discrepancy in hysteresis widths between the smaller, single-domain NPs studied by Lopez et al. and the present experiment suggests that strain also increases with volume by creating additional point defects. This idea will be discussed later in conjunction with the density functional calculations.

Another key feature of Figure 4 is the rate of change of hysteresis width as a function of nanoparticle volume. The slope of this function for the electronic signature of the transition parallels its structural counterpart in both the single and the multidomain regimes. The significance of this result is two-fold: First, it suggests the direct relationship between the number of intrinsic nucleation sites and the energy switching requirement for the NP, in a given size range. Second, the fact that the slope in the multidomain regime is less steep than in the single-domain range suggests that the effect of grain boundaries is to create an enhanced defect concentration in the NP. This decrease in slope for multidomain NPs implies once again that the first grain boundary to be formed dominates the nucleation process.

To further substantiate this model of the interfacial effect, we explored the role of oxygen vacancies in nucleating the observed phase transformation by performing first-principles density functional calculations on the formation energy of these point defects at grain boundaries. It has been shown previously that grain boundaries in polycrystalline materials induce local strains,<sup>35–37</sup> which have a drastic effect on the formation of point defects in metal oxides.<sup>38</sup> Similar effects are expected in VO<sub>2</sub>. To simulate the strain induced by the grain boundaries, the bulk VO<sub>2</sub> was stretched in two dimensions, as in the work of Klie et al.<sup>38</sup> First-principles calculations were performed using the VASP package.<sup>39</sup> The Perdew, Burke, and Ernzerhof-generalized gradient approximation exchange–correlation potential<sup>40</sup> was used, and electron–core interactions were treated in projector augmented wave formalism.<sup>41,42</sup> A rotationally invariant DFT+U approach<sup>43</sup> was applied, and the effective parameters,  $U$  and  $J$ , to include the Hubbard on-site Coulomb repulsion, were specified as 4.0 and 0.68 eV, respectively.<sup>44</sup> Further details of the calculation can be found in the Supporting Information.

As shown in Figure 5, the formation energy of an oxygen vacancy in VO<sub>2</sub> bulk is 3.4 eV. By stretching the bulk crystal along the [100] and the [010] directions by 5%, we found a drop of 0.5 eV indicating that strain induced by the grain boundaries indeed facilitates the formation of oxygen vacancy defects. For grain boundaries at surfaces, the formation energy of a surface oxygen vacancy on the (011) surface, the most stable surface of VO<sub>2</sub> as shown by the surface energy calculations (see Supporting Information), is 1.6 eV. In the presence of 5% tensile strain, the formation energy decreases to 1.3 eV. Therefore, due to the strain-reduced formation energy, one expects that in the multidomain NPs more defects occur at the grain boundaries. The correlation between the increased defect concentration suggested by the calculations, and the lower switching energy required in multidomain NPs found experimentally suggests that vacancies may serve as the nucleation sites for this heterogeneous first-order phase transition<sup>22,45</sup> and, consequently, provides an explanation for the reduced hysteresis width in multidomain NPs.

In principle, delocalization of the strain field over the entire nanoparticle could potentially modify the character of the phase

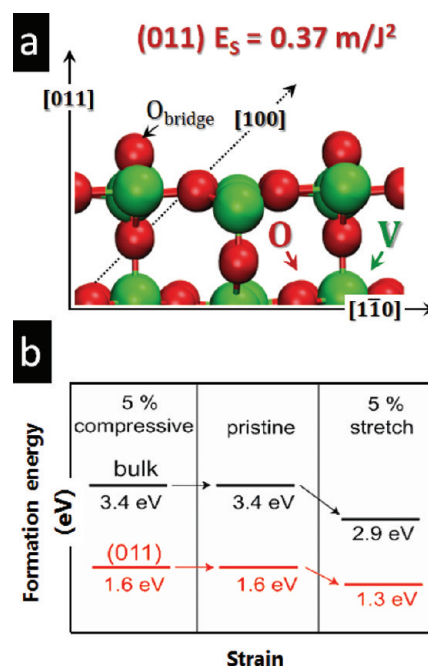


**Figure 5.** First-principles density functional calculations of the formation energy of oxygen vacancies on the most stable (011) surface of VO<sub>2</sub> (a) under various compressive and stretching fractions (b). Both bulk and surface compression and stretching are shown.

transition. However, this possibility is excluded because strain fields around grain boundaries are short-range and localized, decreasing exponentially with distance from the boundary. The range of a grain boundary strain field can be estimated from the spacing ( $D$ ) of the dislocations in the grain boundary,<sup>46</sup> by dividing the Burgers vector by the grain boundary angle in radians.<sup>47</sup> For example, the Burgers vector for the (011) surface is about one unit cell length, that is about 5 Å. Therefore, for a small-angle grain boundary of 10°,  $D$  is about 3 nm. For a large-angle grain boundary of about 60°, found by Yang et al. using transmission electron microscopy, we can estimate that the decay length for the strain field should be even smaller, of a few Ångstroms only.<sup>17</sup> This agrees nicely with the experimental findings of about 2 nm for YBa<sub>2</sub>Cu<sub>3</sub>O<sub>7</sub> as well.<sup>46</sup> Consequently, this phase transition is driven mainly by the accumulation of point defects at grain boundaries.

Although experiments to identify the mechanism of such size-dependent switching have been performed<sup>32,15</sup> following the initial observation by Lopez et al.,<sup>14</sup> the interpretation of the nanoscale VO<sub>2</sub> response, in particular distinguishing electronic and structural transitions, was complicated by the presence of a gold interface. In these experiments, owing to the low signal of pure VO<sub>2</sub> NPs, both in extinction (~10 times less than Au NPs) and Raman spectroscopy, gold nanostructures were employed either as surface enhanced Raman scattering agents<sup>32</sup> or plasmonic nanosensors.<sup>15</sup> This precluded detailed understanding of the mechanism or understanding of the specific point defect. Taken all together, these new experimental and theoretical results make a strong case that the oxygen-vacancy defect triggers the heterogeneous nucleation of the phase transition at the nanoscale. The case rests on three pillars: First, the lithographic fabrication of VO<sub>2</sub> nanoparticles that covers a range of sizes to contain single or multidomain grain; second, the plasmon resonance nanospectroscopy which, combined with full electromagnetic field

simulations, shows how shape and size affect the dipolar plasmon resonance of the intrinsic VO<sub>2</sub> nanoparticle; and third, density functional calculations that show how mismatched or strained VO<sub>2</sub> at grain boundaries modifies the phase transition by reducing the energy required to form the oxygen-vacancy defects.

The implications of these results are two-fold: First, since VO<sub>2</sub> was used here only as a prototypical insulator-to-metal transition, these point defects may suggest a new method for tailoring any general first-order phase transition by preferential nucleation at certain locations.<sup>48</sup> Second, one could also envision an ensemble of NPs of different sizes within one single device, but whose properties could be driven individually and selectively, depending on an engineered interface or defect content. This opens the door for domain-boundary engineering, which could be crucial for the development of nanoscale devices activated by phase transitions.

## ■ ASSOCIATED CONTENT

### ■ Supporting Information

High resolution atomic force micrographs of the VO<sub>2</sub> nanoparticles under study. A detailed explanation of the density functional calculations, together with the surface energies of various other VO<sub>2</sub> facets. This material is free of charge via the Internet at <http://pubs.acs.org>.

## ■ AUTHOR INFORMATION

### Corresponding Author

\*E-mail: [krishenappavoo@gmail.com](mailto:krishenappavoo@gmail.com). Telephone: 001.615.618.4429.

### Author Contributions

<sup>†</sup>These authors contributed equally.

### Notes

The authors declare no competing financial interest.

## ■ ACKNOWLEDGMENTS

The authors thank J. Nag for helpful discussions regarding VO<sub>2</sub>. K.A. was supported by a research assistantship provided by the National Science Foundation (ECE-0801980). Portions of this work were performed at the Vanderbilt Institute of Nanoscale Science and Engineering, using facilities renovated under NSF ARI-R2 DMR-0963361. Research at Imperial College London was sponsored by the Engineering and Physical Sciences Research Council (EPSRC). Y.S. and D.Y.L. acknowledge funding from the Leverhulme Trust. Research at Vanderbilt was supported by DTRA grant HDTRA1-10-1-0016 and computations were performed at the AFRL. Theoretical work was supported in part by the Department of Energy Basic Energy Sciences and the McMinn Endowment.

## ■ REFERENCES

- (1) Zheludev, N. *Nature Photon.* **2007**, *1* (10), 551–553.
- (2) Santander-Syro, A. F.; Copie, O.; Kondo, T.; Fortuna, F.; Pailhes, S.; Weht, R.; Qiu, X. G.; Bertran, F.; Nicolaou, A.; Taleb-Ibrahimi, A.; Le Fevre, P.; Herranz, G.; Bibes, M.; Reyren, N.; Apertet, Y.; Lecoer, P.; Barthelemy, A.; Rozenberg, M. J. *Nature* **2011**, *469* (7329), 189–193.
- (3) Reyren, N.; Thiel, S.; Caviglia, A. D.; Kourkoutis, L. F.; Hammerl, G.; Richter, C.; Schneider, C. W.; Kopp, T.; Rüetschi, A.-S.; Jaccard, D.; Gabay, M.; Muller, D. A.; Triscone, J.-M.; Mannhart, J. *Science* **2007**, *317* (5842), 1196–1199.
- (4) Simpson, R. E.; Fons, P.; Kolobov, A. V.; Fukaya, T.; Krbal, M.; Yagi, T.; Tominaga, J. *Nature Nanotech.* **2011**, *6* (8), 501–505.
- (5) Cilento, F.; Giannetti, C.; Ferrini, G.; Dal Conte, S.; Sala, T.; Coslovich, G.; Rini, M.; Cavalleri, A.; Parmigiani, F. *Appl. Phys. Lett.* **2010**, *96* (2), 021102.
- (6) Yin, W.; West, K. G.; Lu, J. W.; Pei, Y.; Wolf, S. A.; Reinke, P.; Sun, Y. J. *Appl. Phys.* **2009**, *105* (11), 114322–114322–7.
- (7) Yang, Z.; Ko, C.; Ramanathan, S. *Annu. Rev. Mater. Res.* **2011**, *41* (1), 337–367.
- (8) Kim, H. T.; Chae, B. G.; Youn, D. H.; Maeng, S. L.; Kim, G.; Kang, K. Y.; Lim, Y. S. *New J. Phys.* **2004**, *6*, 52.
- (9) Morin, F. J. *Phys. Rev. Lett.* **1959**, *3*, 34–36.
- (10) Eyert, V. *The metal-insulator transitions of VO<sub>2</sub>: A band theoretical approach. Annalen der Physik* **2002**, *11*, 650–704.
- (11) Cavalleri, A.; Dekorsy, T.; Chong, H. H. W.; Kieffer, J. C.; Schoenlein, R. W. *Phys. Rev. B* **2004**, *70*, 16.
- (12) Pashkin, A.; Kubler, C.; Ehrke, H.; Lopez, R.; Halabica, A.; Haglund, R. F.; Huber, R.; Leitenstorfer, A. *Phys. Rev. B* **2011**, *83* (19), 195120.
- (13) Tselev, A.; Luk'yanchuk, I. A.; Ivanov, I. N.; Budai, J. D.; Tischler, J. Z.; Strelcov, E.; Kolmakov, A.; Kalinin, S. V. *Nano Lett.* **2010**, *10* (11), 4409–4416.
- (14) Lopez, R.; Feldman, L. C.; Haglund, R. F. *Phys. Rev. Lett.* **2004**, *93* (17), 177403.
- (15) Appavoo, K.; Haglund, R. F. *Nano Lett.* **2011**, *11* (3), 1025–1031.
- (16) Qazilbash, M. M.; Tripathi, A.; Schafgans, A. A.; Kim, B.-J.; Kim, H.-T.; Cai, Z.; Holt, M. V.; Maser, J. M.; Keilmann, F.; Shpyrko, O. G.; Basov, D. N. *Phys. Rev. B* **2011**, *83* (16), 165108.
- (17) Yang, T. H.; Jin, C. M.; Zhou, H. H.; Narayan, R. J.; Narayan, J. *Appl. Phys. Lett.* **2010**, *97* (7), 072101–072101–3.
- (18) Tselev, A.; Meunier, V.; Strelcov, E.; Shelton, W. A.; Luk'yanchuk, I. A.; Jones, K.; Proksch, R.; Kolmakov, A.; Kalinin, S. V. *ACS Nano* **2010**, *4* (8), 4412–4419.
- (19) Yin, W.; West, K. G.; Lu, J. W.; Pei, Y.; Wolf, S. A.; Reinke, P.; Sun, Y. J. *Appl. Phys.* **2009**, *105* (11), 114322.
- (20) Nagashima, K.; Yanagida, T.; Tanaka, H.; Kawai, T. *J. Appl. Phys.* **2007**, *101* (2), 026103.
- (21) Viswanath, B.; Ko, C. H.; Yang, Z.; Ramanathan, S. *J. Appl. Phys.* **2011**, *109* (6), 063512.
- (22) Lopez, R.; Haynes, T. E.; Boatner, L. A.; Feldman, L. C.; Haglund, R. F. *Phys. Rev. B* **2002**, *65* (22), 224113.
- (23) Fan, W.; Cao, J.; Seidel, J.; Gu, Y.; Yim, J. W.; Barrett, C.; Yu, K. M.; Ji, J.; Ramesh, R.; Chen, L. Q.; Wu, J. *Phys. Rev. B* **2011**, *83* (23), 235102.
- (24) Goncalves-Ferreira, L.; Redfern, S. A. T.; Artacho, E.; Salje, E.; Lee, W. T. *Phys. Rev. B* **2010**, *81* (2), 024109.
- (25) Donev, E. U.; Lopez, R.; Feldman, L. C.; Haglund, R. F. *Nano Lett.* **2009**, *9* (2), 702–706.
- (26) Zhao, L.; Kelly, K. L.; Schatz, G. C. *J. Phys. Chem. B* **2003**, *107* (30), 7343–7350.
- (27) Kelly, K. L.; Coronado, E.; Zhao, L. L.; Schatz, G. C. *J. Phys. Chem. B* **2002**, *107* (3), 668–677.
- (28) Verleur, H. W.; Barker, A. S.; Berglund, C. N. *Phys. Rev.* **1968**, *172* (3), 788.
- (29) Maier, S. A. *Plasmonics: Fundamentals and Applications*, Springer: New York, 2007; p 248.
- (30) Suh, J. Y.; Lopez, R.; Feldman, L. C.; Haglund, R. F. *J. Appl. Phys.* **2004**, *96* (2), 1209–1213.
- (31) Pergament, A. J. *Phys.: Condes. Matter* **2003**, *15* (19), 3217–3223.
- (32) Donev, E. U.; Ziegler, J. I.; Haglund, R. F.; Feldman, L. C. *J. Opt. A: Pure Appl. Opt.* **2009**, *11*, (12), 125002.
- (33) Nag, J.; Payzant, A.; More, K.; Haglund, R. F. *J. Appl. Phys.* **2011**, Apermanent preprint can be found at arXiv:1003.3876, 2010.
- (34) Lei, D. Y.; Appavoo, K.; Sonnefraud, Y.; Haglund, R. F.; Maier, S. A. *Opt. Lett.* **2010**, *35* (23), 3988–3990.
- (35) Ke, M.; Hackney, S. A.; Milligan, W. W.; Aifantis, E. C. *Nanostruct. Mater.* **1995**, *5* (6), 689–697.
- (36) van der Laan, D. C.; Haugan, T. J.; Barnes, P. N. *Phys. Rev. Lett.* **2009**, *103* (2), 027005.

- (37) Wang, B.; Puzyrev, Y.; Pantelides, S. T. *Carbon* **2011**, 49 (12), 3983–3988.
- (38) Klie, R. F.; Buban, J. P.; Varela, M.; Franceschetti, A.; Jooss, C.; Zhu, Y.; Browning, N. D.; Pantelides, S. T.; Pennycook, S. J. *Nature* **2005**, 435 (7041), 475–478.
- (39) Kresse, G.; Furthmüller, J. *Phys. Rev. B* **1996**, 54 (16), 11169–11186.
- (40) Perdew, J. P.; Burke, K.; Ernzerhof, M. *Phys. Rev. Lett.* **1996**, 77 (18), 3865.
- (41) Kresse, G.; Joubert, D. *Phys. Rev. B* **1999**, 59 (3), 1758.
- (42) Blochl, P. E.; Jepsen, O.; Andersen, O. K. *Phys. Rev. B* **1994**, 49 (23), 16223–16233.
- (43) Liechtenstein, A. I.; Anisimov, V. I.; Zaanen, J. *Phys. Rev. B* **1995**, 52 (8), R5467.
- (44) Biermann, S.; Poteryaev, A.; Liechtenstein, A. I.; Georges, A. *Phys. Rev. Lett.* **2005**, 94 (2), 026404.
- (45) Maiti, A.; Pantelides, S. T.; Chisholm, M. F.; Pennycook, S. J. *Appl. Phys. Lett.* **1999**, 75 (16), 2380–2382.
- (46) Zhi-Xiong Cai, Y. Z. *Microstructures and Structural Defects in High-Temperature Superconductors*; World Scientific Publishing Co., Inc.: Hackensack, NJ, 1998.
- (47) John Price Hirth, J. L. *Theory of Dislocations*. Krieger Publishing Co.: Malabar, FL, 1992.
- (48) Salje, E. K. H. *Phase Transitions in Ferroelastic and Co-Elastic Crystals*. Cambridge University Press: Cambridge, U.K., 1990.